Multimedia Tools and Applications
https://doi.org/10.1007/s11042-024-20241-8

ADRGS: an automatic diabetic retinopathy grading system through machine learning

Y. Aruna Suhasini Devi[1] · **K. Manjunatha Chari**[2]

Received: 29 September 2022 / Revised: 25 July 2024 / Accepted: 5 September 2024
© The Author(s), under exclusive licence to Springer Science+Business Media, LLC, part of Springer Nature 2024

Abstract
In recent years, Diabetic Retinopathy (DR) has emerged as a significant chronic ailment affecting roughly one-third of diabetic patients globally. DR is the leading cause of vision impairment and detecting DR in its early stages can be a challenging task, but if neglected, it can lead to severe DR and, ultimately, permanent vision loss. Therefore, the development of an automated DR detection system, based on retinal fundus images is of paramount importance. This paper develops an automatic Diabetic Retinopathy (DR) screening system that analyzes the fundus retinal images and produces a grade to determine the severity of DR by using computer vision and machine learning algorithms. The complete system is four-fold; pre-processing, segmentation of the vessels and optic disc (OD), lesions classification and grading the severity of DR. The initial pre-processing phase enhances the quality of retinal image based on the spatial collaboration between pixels. The second phase segments the retinal vessels and Optic Disc through mathematical morphology and composite filtering strategy. The third phase performs classification of the entire image into four types of lesions namely Hard Exudates (EX), Hemorrhages (HM) and Microaneurysms (MA) and Cotton Wool Spots (CWS). At this phase, each pixel is represented with a set of 30 features including 14 structural features and 16 appearance based features. A two-step hierarchical classification method is employed to classify the image into lesions and sub lesions. Finally, the classification results are formulated as a function to determine the severity of DR. For validation purposes, DIARETDB1 database is used, and the performance is measured through the parameters: Specificity, Sensitivity, Area under Curve (AUC) and Accuracy. For feasibility checking, three machine learning algorithms are employed namely Gaussian Mixture Model, K-Nearest Neighbor and Support Vector Machine.

Keywords Diabetic retinopathy · Retinal images · Vessels · Optic disc · Lesions · Composite features · Accuracy · AUC

Extended author information available on the last page of the article

1 Introduction

Recently, Diabetic Retinopathy (DR) has been found to be one of the most complicated diseases due to neglected diabetes. DR patients are found to be increasing linearly and occupying approximately a third portion of diabetic patients over the entire world. DR is a found to be a progressive disease and consequences to permanent vision loss if untreated. According to the American Diabetes Association (ADA) survey, DR effected approximately 44,00,000 Americans in the age around 40 and above within the span of four years, i.e., from 2005 to 2008. Approximately 4.4% (1,93,600) of the effected are found to have suffered with the advanced stages of DR which can cause permanent vision loss [1]. By the year 2030, the total DR patients' count is approximated as 191 million [2] while it is estimated to increase to 642 million by the year 2040 [3]. Moreover, it is approximated that DR affects one person for every three persons. Early detection and treatment of DR is essentially required as it can control the risk of vision loss up to 90% [4]. Hence, the need for cost-effective DR diagnosis system has emerged [5]. However, most of the people suffering from diabetes do not prefer any screening test as there is lack of sufficient eye specialists and prolonged manual diagnosis. Hence, the design of a cost effective and automatic DR diagnosis system through the analysis of fundus images is seriously needed [6]. Usually, the signs and characteristics of DR are analyzed through different attributes of retinal images including Neovascularization (NV), Venous Loops (VL), Exudates (EX), Hemorrhages (HM) and Microaneurysms (MA) [7]. The presence of one or more of these attributes in the retinal images signifies the presence of DR. In the initial stages of DR, the patients are usually with no noticeable symptoms, however, in advanced stages, patients suffer from several symptoms including blurred vision, distortion and progressive visual loss. Based on the symptoms, the DR grades are categorized into: Proliferative DR (PDR) and Non-Proliferative DR (NPDR). Further, the NPDR is sub-categorized into three subgrades namely Mild, Moderate and Severe. The presence of MA's indicates mild NPDR, moderate NPDR is indicated by the presence of HM and/or EX and severe NPDR is indicated by the rise in retinal ischemia through the appearance of abnormal, weak and small blood vessels which can also be called as NV. Finally, the PDR is termed as severe stage of DR. Figure 1 shows the different stages of DR through retinal image attributes.

HM looks like MA if they are smaller in size while MA resembles HM if it is larger on the wide blood vessels. In general, the physician differentiates between these two signs by injecting a fluorescein dye into the patient's body. In such cases, the MA turns white color like blood vessels, but HM does not. EX is one more pathological sign which results due to the breakdown of the blood retina barrier that allows the leakage of lipids and proteins from the blood vessels. NV is the major sign of PDR which often occurs nearer to the Optic Disc (OD) and it is termed as NV of the Disc (NVD). If NV occurs within three-disc diameters of the OD, then it is called NV elsewhere (NVE). There exist several schemes to identify the ocular abnormalities in retina that can help the ophthalmologists in the diagnosis of ocular diseases. Previously, Fluorescein Angiography (FA) dye was mostly used for the identification of ocular diseases but later a new method called Fundus Auto Fluorescence (FAF) was used. In the year 1990, the Optical Coherence Tomography (OCT) has been invented to observe the layers of retina. OCT's main intention is to identify the Choroidal NV and Macular diseases in the eye [8]. Recently OCT angiography (OCTA) has been introduced which does not require dye injection and hence it is said to be non-invasive in nature. However, it works only in the smaller sized Field of View (FOV) and they cannot identify the leakages. Based on these studies, it can be said that the color fundus

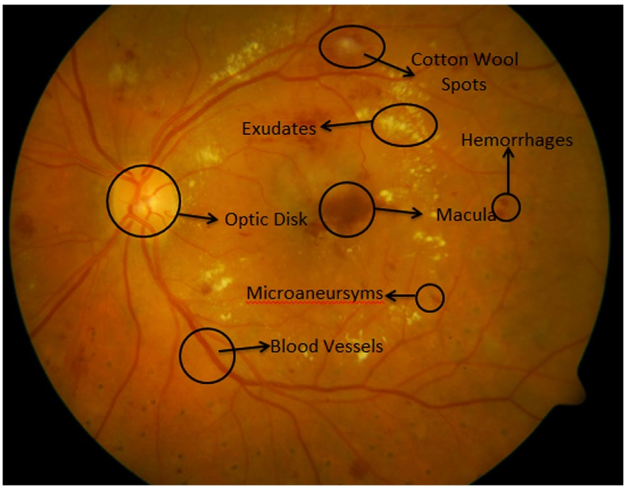

Fig. 1 Retinal image with different DR attributes

image-based DR diagnosis is the most eligible method, which is totally non-invasive, and efficient in the detection of retinal abnormalities [9].

Computer aided screening has recently gained much significance and different methods have been developed for automatic identification of EXs, HMs, and MAs. A. Osareh et al. [10] assumed that MAs are the main indicators of DR and developed a three stage DR diagnosis system with contrast enhancement and color normalization at pre-processing stage, Image segmentation based on Fuzzy C-Means (FCM) Clustering and classification of non-lesions from bright lesions. Recently, Z. Li et al. [11] developed a deep learning algorithm (DLA) for the Automatic Detection of DR (PDR, Diabetic Macular Edema and both). To train and test the system, retinal images in the compact form were considered but segmentation or feature extraction mechanism was not considered.

Unlike the above methods, this paper develops a novel computer aided DR screening system in three phases. In the first phase, this work focuses on Quality and contrast enhancement, in the second phase, removal of background regions (OD and Blood Vessels) is focused and in the third phase, classification of lesions and severity grading of DR is executed. The major contributions of this paper are stipulated as follows.

1. To improve the quality of retinal images, this work proposes a new contrast enhancement mechanism based on the mutual dependency between the adjacent gray levels.
2. To remove the background regions such as Optic Disc and Blood Vasculature, this work proposes a new and simple segmentation mechanism based on mathematical morphology and composite feature extraction filter. This contribution employs mathematical morphology for vessels segmentation and three filters such as Gaussian, Median and Variance filters for Optic Disc seed point determination.
3. The third contribution aims at the classification of retinal lesions such as EX, HM, MA, and Cotton Wool Spots (CWS). A hybrid feature extraction method is proposed which integrates pixel intensity and structural features. The pixel-based feature alleviates the illumination and intensity variations while the structural features alleviate the shape and size information.

4. The final contribution is made at severity grading, and it is executed based on the count of lesions such as EX, HM, MA, and CWS.

Organization of paper Section I discusses the basic details such as the reason for DR, worldwide growth of DR, problem identification, motivation, methodology and objectives. The rest of the paper is organized as follows; section II explores the details of the Literature Survey. Section III explores the details of proposed DR diagnosis mechanism in three phases such as pre-processing, background region removal and foreground regions classification followed by severity grading. Section IV explores the experimental result details and section V concludes the paper.

2 Literature survey

Several researchers developed different methods for the diagnosis of DR based on different methodologies. Brain et al. [12] proposed a three-phase methodology composed of pre-processing, segmentation, and lesions extraction. At pre-processing they employed Contrast Limited Adaptive Histogram Equalization (CLAHE) [13] for enhancing the contrast of retinal images. The Optic Disc was then segmented from contrast enhanced image. Finally, the resulting image was subjected to the extraction of HM and EX based on the Gabor filter, Circular Hough Transform and Thresholding. However, grading of DR was not specified based on the results obtained for EX and HM.

Atlas and Parasuraman [14] employed pixel level classification for DR diagnosis based on the HM. The HM was extracted through three sets of filters namely Gary Level Run Length Matrix (GLRLM) [15], Gray Level Co-occurrence Matrix (GLCM) [16], Speed Up Robust Features (SURF) [17]. For training and testing, an Adaptive Neuro-Fuzzy Inference system (ANFIS) was used but determining HM alone was not sufficient for the diagnosis of DR grades. Orlando et al. [18] employed Support Vector Machine (SVM) on retinal images to extract the blood vessels. They measured pairwise interactions with the help of pixel's distances and a 2D Gabor filter was employed to standardize the image. However, they did not consider the annotated segmentation which has large impact in the negative results. As the line detectors are linear in shape, they could not provide information about the uneven shaped lesions.

Fadafen et al. [19] focused on the extraction of Exudates after the removal of background regions such as OD from retinal image through mathematical morphology. Blood vessels extraction was done based on the three edge features such as Brightness, Width and Direction. But, obtained features are purely based on the Human Visual System (HVS) and are much more sensitive to pixel intensities. However, EX alone is not adequate for the diagnosis of DR. D.W. Safitri and Juniati [20] applied matched filtering and thresholding for the segmentation of blood vessels from retinal images after enhancing their quality through CLAHE. Further, Box-counting method [21] was employed for the assessment of fractal dimensions and K-Nearest Neighbor (K-NN) algorithm was used for classification. However, the discrimination between OD and Hard exudates was not considered.

Abdelmaksoud et al. [22] employed a Multi-Label Classification method for the diagnosis of DR grades from retinal images. Initially, they processed the retinal images for noise elimination followed by quality enhancement through Histogram Equalization based on Dynamic Stretching method. Then they segmented four pathological regions

from retinal images including MA, HM, EX and Blood Vessels. Six different features are extracted through Gray Level Co-occurrence Matrix (GLCM), blood vessels bifurcation points and four extracting regions. Finally, these features were given to SVM classifier for classifying the normal and several grades of DR. However, GLCM could not determine the shapes of retinal lesions as they were of different shapes and sizes.

Recently, deep learning has gained huge significance in different applications and some of the authors applied deep learning methods for DR diagnosis. Compared to machine learning algorithms, deep learning has the major advantage of no separate feature extraction. M. D. Abramoff et al. [23] employed the IDx-DR [24] device's software which considers the Macula and OD as inputs for grading of DR. IDx-DR device's major sources are AlexNet [25] and Oxford Visual geometry. They transformed the IDx-DR device, to be applicable for real time retinal image datasets. However, their methodology was unable to identify the advanced stage of DR from Macular Edema.

Bellemo et al. [26] formulated an integrated deep learning model for DR diagnosis by integrating two CNN models such as VGGNet [28] and ResNet [27]. They applied a gradient descent model for classifying the retinal images. For a given input image, both the deep learning models produced an individual output, and results were derived based on their fusion. Even though they achieved better performance in segmentation, the combined result had a huge computational burden on the system. Mansour [29] employed the most popular Deep learning model, i.e., AlexNet for extracting the blood vessels from retinal images. Connected Component Analysis (CCA) [30] was employed for the extraction and selection of features. After feature extraction, SVM was employed for classification of images to determine the grade of DR. As the abnormalities in blood vessels are observed only in the PDR, it cannot support grading of DR. Gadekallu et al. [31] and Zou and Xue [32] employed Principal Component Analysis (PCA) for the dimensionality reduction and firefly algorithm was used for the optimization of parameters.

Inception-V3 [34] is one of the popular deep learning methods which gained a first runner up on the ImageNet Large Scale Visual Recognition Competition (ILSVRC). Based on its positive outcome, Hagos et al. [33] employed it for the detection of DR through retinal images. Data insufficiency problem was solved by sub-sampling the smaller version of Kaggle DR Classification challenge dataset for model training and tested with unseen dataset. Similarly, Tymchenko et al. [35] also employed an Efficient-Net called deep learning mechanism for DR diagnosis which works basically on the ImageNet [36] framework. At first, the retinal image is processed through several transformations including vertical flipping, Transposing, and Rotation. They suggested using Shapley Additive Explanation (SHAP) [37] for the visualization of features which assist the physicians in the DR diagnosis in future. The retinal images were fed directly to deep learning model without extracting any DR related attributes, hence classification of DR based on attributes was not performed. Such kind of mechanism works only on limited images.

Xu et al. [38] suggested a deep CNN model with ten convolutional layers, five max pooling layers and one fully connected layer to identify the presence of DR in retinal images. They employed SoftMax classifier and SGD optimizer and applied an image augmentation at pre-processing stage. However, they performed their method's validation using few sets of images which cannot explore the robustness. Pratt et al. [39] also suggested a deep 13-layered CNN model with three fully connected layers and ten convolutional layers. Rectified Linear Unit (ReLU) is employed as an activation function, and determined five

grades of DR. Since pre-processing of retinal images was neglected, their method showed poor performance for noisy retinal images.

Summary of problem From the past literature survey, it was found that most DR diagnosis systems are incomplete. Real time images require pre-processing as they consist of noise, colour distortions, etc., but most of the methods did not concentrate on the pre-processing as it constitutes an extra burden on the system. An example of such kind of methods are [6] and [40] which have rejected approximately 18% and 5% retinal images respectively due to their bad quality. Most of the existing methods found it complex to extract continuous boundary of OD due to its discontinuity and high gray-level intensity variations. The proposed method outperformed the conventional methods by accurately identifying the ODP through statistical analysis in order to segment OD region accurately. Some methods applied lesions segmentation without segmenting the OD, which comprises the major attribute of retinal image. The segmentation of only retinal vessels constitutes an increased misclassification due to the correlation between pixels of OD and bright lesions. Some of the methods applied only vascular segmentation which can identify minor vessels effectively, but the blood vessels do not contribute any information to the mild and moderate grading of DR.

3 Proposed approach

3.1 Overview

Here in this section, the details of the proposed system are explored clearly. Accordingly, the overall system is accomplished in three phases; they are pre-processing, background region segmentation and foreground region classification. At the pre-processing stage, the low-quality retinal image is subjected to quality enhancement. A new contrast enhancement technique called SCCE is employed which considers the mutual relationship between pixels to adjust their contrast levels. SCCE considers only green plane of retinal image for contrast enhancement. Further, in the second phase, the background regions (Blood vessels and Optic Disc) are segmented from contrast enhanced green plane of retinal image. Two separate mechanisms are applied for the segmentation of vessels and Optic Disc. Once the background regions are segmented, they were combined with red and blue plane of the image and the resultant image is called as lesions sub-image as it consists of only lesions. In the last phase, the lesion image is processed for lesions classification by employing a two-level hierarchical classification. Finally, based on the lesions count obtained, grade of DR is determined according to the clinical standards. The overall working schematic of proposed DR diagnosis system is shown in Fig. 2.

3.2 Pre-processing

The main intention of pre-processing is to enhance the quality of low-quality retinal images to obtain a clear view of retinal attributes such as vessels, Optic Disc and Lesions. For accurate diagnosis of DR, a novel contrast enhancement method called Spatial Collaborative Contrast Enhancement (SCCE) is used which enhances the contrast of retinal image to visualize attributes of retinal image such as vessels, optic disc, exudates etc. Initially, the green plane is extracted from RGB color image and then it is applied for Spatial

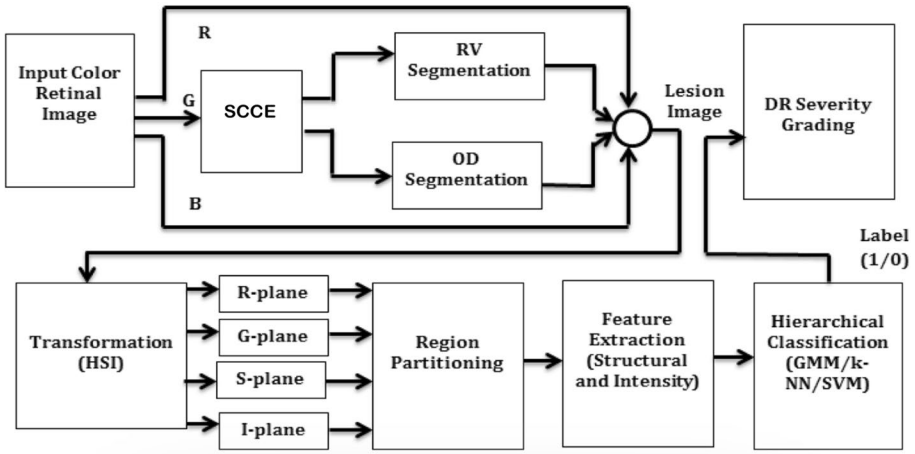

Fig. 2 Overall working schematic of proposed DR diagnosis system

Collaborative Contrast Enhancement (SCCE) [41]. SCCE considers the spatial mutual dependency between the pixels of image to adjust their contrast levels. SCCE initially divides the image into numerous blocks of equal sizes overlapping in nature. Partitioning is done in such a way that; every pixel must be the center pixel of at least one block. The obtained blocks are called grid, and the process is called spatial grid sliding because the grid slides over the entire image to partition it. Then histogram and entropy are computed for each block. The histograms are normalized by the block size and then subjected to Spatial Collaboration Computation.

Let's assume two gray levels a_g and b_g and the corresponding histograms are $h_a(t,s)$ and $h_b(t,s)$ where $1 \leq t \leq T$ and $1 \leq s \leq S$, T and S are the size of block. Then the Joint Spatial Histogram (JSH) between these two gray levels is signified as $h_{a,b}(t,s)$ determines the co-occurrence of two gray levels on a grid and it is calculated as

$$h_{a,b}(t,s) = \text{average}(h_a(t,s), h_b(t,s)) \tag{1}$$

where $h_{a,b}(t,s)$ denotes the JSH between two gray levels at t and s. JSH determines the joint relation between two gray levels which can help in identifying the homogeneous regions in the retinal image. Based on the obtained JSHs, the Spatial Collaboration (SC) between two gray levels is computed through the mutual information existing between them. Let $I_{a,b}$ be the Spatial Collaboration Coefficient, computed as

$$I_{a,b} = \sum_{t=1}^{T} \sum_{s=1}^{S} h_{a,b}(t,s) \ \log_2 \left(\frac{h_{a,b}(t,s)}{h_a(t,s) h_b(t,s)} \right) \tag{2}$$

Based on the obtained $I_{a,b}$ value, the spatial collaboration between two gray levels is determined. When the occurrence of two gray levels is nearly same over a grid, then the SC is observed to be high. Hence larger gaps are allocated between the two output gray levels so that the contrast obtained for the output retinal image is superior to that of the input retinal image. On the other hand, if SC is observed to be less between the two gray levels, then their occurrence is much deviated. Under such a condition, even a small gap can visualize the gray levels effectively. Hence, based on the obtained SC values between each

gray level, the SCs are sorted, and ranks are assigned based on their magnitudes. Finally, the contrast of a pixel in the output image is adjusted by mapping process which is done as a linear combination of input pixel gray level and the average rank between adjacent gray levels.

3.3 Background regions segmentation

Once the retinal image is pre-processed, it is subjected to background region segmentation. Since the retinal vessels are major parts in the diagnosis of advanced stage of DR, the extraction of complete retinal vasculature from fundus images is crucial. A new vessel segmentation mechanism in three stages is proposed. Initially, major blood vessels are extracted from the colour retinal image and in the second phase, composite feature extraction is employed to extract the minor blood vessels accurately, followed by post processing in the third stage. The proposed method differentiated and extracted almost entire vessel structure with more accuracy. In this phase, the Blood vessels and Optic Disc are treated as background regions while the lesions are considered as foreground objects. Two different methods are applied for the segmentation of both vessels and OD. The details are explored in the following subsections.

3.3.1 Blood vessels segmentation

Blood Vessels Segmentation is executed in three stages, they are major blood vessel extraction, minor blood vessel classification and post processing. Initially, the retinal image is processed for major blood vessels segmentation and then for minor blood vessels segmentation. After completing segmentation of major and minor vessels, post processing is done to obtain the final vessel structure.

A. Major blood vessels

Consider I_E to be the enhanced image (output of SCCE). Initially, it is subjected to normalization to get the pixel intensities in the range of [0 1]. Let I_N be the normalized image, it is smoothened through a Low Pass Filter (LPF) and then subtracted from its original version to get the High Pass Filtered Image H. Then H is thresholded (using Eq. (4)) against threshold p to get the binary image denoted as H_1.

$$H(x,y) = abs(I_N(x,y) - LPF\big(I_N(x,y)\big) > 0) \tag{3}$$

$$H_1(x,y) = \begin{cases} 1;\ if\ H(x,y) > p \\ 0;\ Otherwise \end{cases} \tag{4}$$

Next, the regions corresponding to the dark pixels are extracted from the negative of normalized image and let the resultant image be denoted as I_R. Then, the I_R is subjected to top-hat transform [42] to construct totally 12 top-hat reconstructions. For each reconstruction the length of the linear structuring element is assigned 15 pixels and width is 1 pixel. The angular deviation maintained between each reconstruction is 15^0 and it begins from 0° and ends in 180^0. Then the final image is constructed by choosing the maximum intensity

value among 12 reconstructions and it is denoted as T. Then T is subjected to thresholding against p. The Top-hat reconstruction and thresholding is done according to the following equations.

$$I_R = (1 - I_N) \circ g \tag{5}$$

$$T_{i,i=1to12} = TopHat\left(I_R^{\theta}\right), \theta = 0^0 : 15^0 : 180^0 \tag{6}$$

$$T(x,y) = \max\left(T_i\right), i = 1\ to\ 12 \tag{7}$$

$$T_1(x,y) = \begin{cases} 1;\ if\ T(x,y) > p \\ 0;\ Otherwise \end{cases} \tag{8}$$

where Eq. (5) explores the morphological opening operation between a structuring element g and inverse of normalized contrast enhanced green plane of retinal image. It removes small objects from the foreground (usually taken as bright pixels) of an image, placing them in the background. The final major blood vessel structure (M) is obtained by the fusion of H_1 and T_1 as follows.

$$M = H_1 \cap T_1 \tag{9}$$

B. Minor blood vessels extraction

Once the major blood vessels are removed from two binary images such as H_1 and T_1, the resultant is minor vessel image denoted as H_1' and T_1', obtained as [43].

$$H_1' or T_1' = \begin{cases} 1;\ if\ M(x,y) = 0\ and\ H_1(x,y)\ or\ T_1(x,y) = 1 \\ 0;\ Otherwise \end{cases} \tag{10}$$

Based on H_1' and T_1' the Minor vessel image (C) is derived as follows.

$$C(x,y) = \begin{cases} 1;\ if\ H_1'(x,y) = 1\ and\ T_1'(x,y) = 1 \\ 0;\ Otherwise \end{cases} \tag{11}$$

Next C is subjected to pixel level classification through machine learning algorithms. Initially, it is subjected to feature extraction of five sets of features including Gradient Features, Hessian Features, Statistical Features, Morphological Features and Edge Features. Each pixel is represented with a total of 16 features among which 2 are Gradient, 3 are Hessian, 8 are statistical, 2 morphological and 1 edge feature. Gradient gives information about the image and are calculated in two directions, i.e., horizontal and vertical directions and the final gradient and the corresponding direction are measured. Each pixel is produced with four gradient features, they are G_x, G_y, G_M and G_θ. In the Gradient domain, the pixel is represented with gradient magnitude and gradient direction. Hessian matrix is constructed with the help of second order derivatives that are very useful in the extraction of minor vessels as they can separate vessel pixels from background pixels much effectively. The three Hessian features include G_{xx} and G_{yy} which are the second order gradients of image in x and y- directions respectively and G_{xy} is the second order gradient dependent on the y parameter in the x- direction. Under statistical Features, 8 features are calculated for each

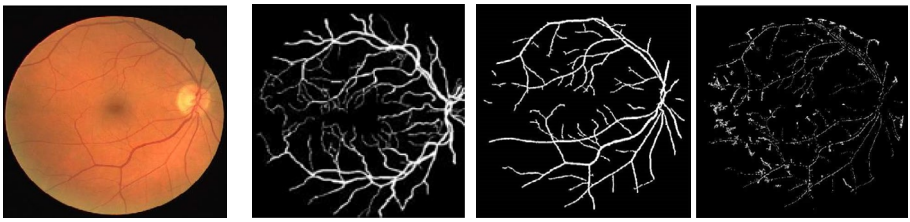

(a) (b) (c) (d)

Fig. 3 (**a**) Color image (**b**) Ground truth vessels (**c**) Major blood Vessels and (**d**) Minor blood vessels

pixel based on the sliding window with the candidate pixel placed at the center of window. For every window totally 8 features are measured, they are Mean, Maximum, Minimum, Standard Deviation, Mean Absolute Deviation (MAD), RSS, Skewness, and Kurtosis. Two morphological features include Morphological opening and closing with a linear structuring element of 15-pixel length. To differentiate perfectly between vessel pixels and background pixels top-hat and bottom-hat transforms were applied. Top–hat transform extracts brighter areas and acts like HPF, while the darker regions are extracted by the bottom hat transform. Finally, the edge features are obtained from the derivatives of five edge operators that include Roberts, Prewitt, Sobel, Canny and Laplacian of Gaussian (LoG). Roberts operator calculates the gradient value and specifies the high frequency range that explores the edge related information. Prewitt operator finds the difference in intensity values of neighbor pixels in both x- and y- directions. Sobel operator is similar to Prewitt, but it emphasizes more on the pixels that are close to the center of mask. Canny operator is a more powerful edge operator that determines the corner points which have three possible gradients that are horizontal, vertical, and diagonal. LoG removes the unnecessary regions due to the presence of noise in the minor vessel image. For classification, SVM algorithm is employed with Radial Basis Function Kernel. Figure 3 shows an example of original color image, ground truth vessel image, major blood vessels and minor blood vessels.

3.3.2 OD segmentation

For accurate diagnosis of DR, OD region analysis is essential and hence, a new OD segmentation technique based on Composite Filtering and Mathematical Morphology is proposed. For accurate segmentation, the blood vessels need to be removed. A linear and rotating structuring element (SE) is applied on every pixel in the sub-image to compute the maximum variance after performing one rotation through SE. OD segmentation involves two phase methodology consisting of OD Pixel (ODP) detection followed by segmentation. Here, the main seed of the OD is used to obtain the ODP. To accomplish this task, three different methods are employed namely Median Filtering method, Variance Filtering method and Gaussian Filtering method [44]. For every method, one probable location of ODP is obtained and the final ODP is detected based on its relationship with the centroid calculated as an average of three locations. The selection is as follows: 1) The centroid itself becomes the ODP if the three possible locations are closer to it. 2) If two locations among the three locations are nearer to the centroid, then the average of two locations is considered as ODP. Figure 4 shows the results of OD segmentation.

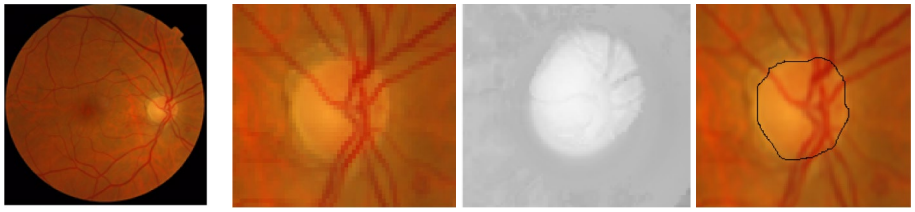

(a) (b) (c) (d)

Fig. 4 (**a**) Color image, (**b**) Vessel Sub-image, (**c**) Vessel removed sub-image and (**d**) Segmented OD

In the median filtering method, a 21×21 sized median filter is applied over retinal image's green channel. Then the maximum difference is determined for every window as the difference of minimum grey-pixel intensity and maximum pixel intensity. Typically, the brightness of OD region is better than other regions and highest gray-level variations occur within the OD region. Consider windowed median filtered image as $\left(I_M\right)_{W,}$ and the mathematical expression for obtained OD pixel location is given as

$$P_M = \underset{(i,j)}{\arg}\left[\max(d(i,j))\right] \tag{12}$$

where

$$d(i,j) = \left[\left(I_M\right)_W^{max}(i,j) - \left(I_M\right)_W^{min}(i,j)\right] \tag{13}$$

Under Variance filtering method, each pixel's statistical variance is determined for the green channel of retinal image. Here, Maximum pixel variation is taken into consideration to locate the OD pixel in the windowed image of size 51×51. Consider windowed image as I_W, and $\overline{M}$ as the mean, the mathematical expression for obtained OD pixel location is given a

$$P_V = \underset{(i,j)}{\arg}\left[\max(V(i,j))\right] \tag{14}$$

where

$$V(i,j) = \frac{\sum_{i=1}^{51}\sum_{j=1}^{51}\left(I_W(i,j) - \overline{M}(I_W)\right)^2}{L\left(I_W\right) - 1} \tag{15}$$

Under Gaussian Filtering method, the Gaussian LPF is considered and applied on the transformed image. The candidate pixel in the transformed domain is calculated as

$$P_G = \underset{(i,j)}{\arg}\left[\max(G(i,j))\right] \tag{16}$$

where

$$G(i,j) = exp\left(\frac{-d^2(i,j)}{2d_0^2}\right) \tag{17}$$

where d_0 is signified as cut-off frequency and d^2 is signified as the Euclidean distance between two pixels at locations i and j.

After deriving the ODP, the OD region is segmented from the sub-image of size 400×400 cropped from the original image. The sub-image consists of blood vessels as OD is the seed point of blood vessels. With the presence of blood vessels, the OD segmentation becomes incomplete. Hence, for an accurate segmentation, the blood vessels need to be removed. In general, the retinal vessels are considered as linear elements with length L and width W subjected to $(W << L)$. As the pixels along the linear shape are almost similar because the major blood vessels look much darker, and it is totally opposite to the pixels of OD. Based on these assumptions, a linear and rotating structuring element (SE) is applied on every pixel in the sub-image. The width of element is considered as 1 and length is considered as l_1 and the gap between each rotation is maintained as 20^0. For each pixel, the maximum variance is computed after performing one rotation through SE. The mathematical representation is shown as

$$I_n(i,j) = \max_{(i,j)} \left(I_{SE}^{\theta}(i,j) \right) \tag{18}$$

where I_n is the non-vessel sub-image, θ is the rotation angle, and the term $\max_{(i,j)}(.)$ produces a maximum value in the output at the rotation of θ. As this process considers the variance instead of gray-level pixel intensity, it is mathematically derived as

$$V(i,j) = Var(I_{SE}^{\theta}(i,j)), k = 1,2,\ldots,9) \tag{19}$$

From the above equation, the occurrence of maximum variance at the rotation angle is formulated as

$$\theta = \arg_{(k)} \left(\max(V_k(i,j)) \right) \tag{20}$$

3.4 Lesions classification

To analyze the lesions for DR diagnosis, a new method is proposed which applies a pixel level classification. After segmenting the background regions from the green plane of input retinal image, the residual image is called lesion image, and it is concatenated with remaining R and B planes to form the compete color fundus image. The lesion image is subjected to region partitioning and then every region is processed for feature extraction followed by classification, achieved by training the system through a machine learning algorithm. The feature selection is a random process. A total of 20 structural features were extracted from retinal image through CCA. However, maximum performance was observed at 14 structural features and 16 intensity-based features. It is then subjected to lesions classification through a two-phase methodology composed of feature extraction and classification in a hierarchical fashion. The system is trained through a machine learning algorithm to classify the pixel into four classes. They are: CWS, HE, HM, and MA. The classification is done in two stages; the first stage classifies the regions into true lesions and non-lesions while the second stage further classifies true lesions into sub-classes to enable the grading mechanism. Totally two types of lesions are considered, they are bright lesions and red lesions. For every

Table 1 Structural Features and their description

Name of feature	Description
Area	Total pixels present in the region
Distance from ODP	Distance between center pixels in current and OD regions
Major Axis length	Length of Ellipse's Major axis
Minor Axis length	Length of Ellipse's Minor axis
Length	Length of a rectangle bounded the region
Width	Width of a rectangle bounded the region
Diameter	Diameter of a Circle surrounded the region
Euler Number (e)	$e = \sum_{n=0}^{n_p} \frac{1}{n!}$
Solidity	Ratio of the area to the convex area
Perimeter	Total pixel distance around the region
Orientation	Angle between major axis of ellipse and horizontal axis
Filled area	Area region after filling all holes
Vascular Distance	Distance between the vessel region's center pixel and current region's center pixel
Eccentricity	Ellipse's normalized 2^{nd} central movements

region, 30 features were totally extracted and applied to classifier. For classification purposes, three algorithms namely SVM, K-NN and Gaussian Mixture Model (GMM) were employed.

3.4.1 Region partitioning

In this phase, the lesion image is subjected to region partitioning, by dividing the image into small sized regions. To achieve such division, a spatial widow is applied over the image thereby making every pixel as a center pixel. If I_L is assumed as lesion image, then a region with center pixel at *(x, y)* is denoted as $\left(I_L\right)_R(x, y)$. The region partitioning is done on totally four different planes of lesion image; they are Red plane (R), Green plane (G), Intensity plane (I) and Saturation plane (S). As the main intention is to identify all the possible lesions, the HSV transformed image is also considered for computation. Moreover, each plane has its own contribution towards the provision of sufficient information about lesions. For example, the saturation and intensity planes well demonstrate the characteristics of bright lesions while the red lesions are well characterized through red and green planes.

3.4.2 Features

For feature extraction, a total of 30 features are considered among which 16 are pixel intensity based and the remaining 14 are structure oriented. Even though some methods employed pixel level classification through different features, they had shown limited performance as they considered only limited set of features. For instance, A. Frame et al. [45] employed Spencer-Frame system on each pixel and extracted a total of 13 features. Later they extended the method to extract 68 features [46] to determine if the pixel is carrying lesions or not. An example of pixel intensity-based feature is mean, and an example

Table 2 Pixel Intensity Features and their description

Name of feature	Description
Mean	$\mu_i = mean\{(I_L)_R\}^i, i \in \{G,R,S,I\}$
Variance	$v_i = variance\{(I_L)_R\}^i, i \in \{G,R,S,I\}$
Minimum	$\alpha_i = min\{(I_L)_R\}^i, i \in \{G,R,S,I\}$
Maximum	$\delta_i = max\{(I_L)_R\}^i, i \in \{G,R,S,I\}$

of structure-based feature is solidity. Table 1 shows the details of structural features and Table 2 shows the details of pixel intensity-based features.

In the case of pixel-based feature extraction, the region of each plane is processed for mean, variance, maximum and minimum features. Hence, the total number of features used to represent each region is 16. Finally, each region is represented with a total of 30 features. Even though the feature count is larger, every feature has significance in demonstrating the characteristic of lesions. For instance, the distance between center pixels of EX and CWS regions is larger compared to the center pixels of non-lesion regions. In the case of red lesions, they locate far from the blood vessels than the non-vessel regions. Hence, the distance between the region of vascular regions and non-lesion regions is small. As the lesion regions have no blood vessels they lie only in the non-lesion's region. Hence, the length of major axis of non-lesion regions is more compared to the lesion regions as the blood vessels are of elongated structure. During the second stage of classification, the pixel-based features provide much discrimination between EX and CWS as the EX-pixels are brighter than CWS pixels. Moreover, the area compactness of CWS regions is signified by the structural feature called solidity.

3.4.3 Classification

At the classification phase, a two-step hierarchical classification is applied. Here the lesion image (I_L) is composed of two types of lesions namely bright lesions (B_L) and red lesions (R_L). Consider the $(I_L)_R$ to be one region of I_L, then the first stage classifies it into two classes; they are True Lesions ($(I_{TL})_R$) and False Lesions ($(I_{FL})_R$). Assume the Bright lesion region as $(I_{BL})_R$, upon classification, the True and False bright lesion region is denoted as $(I_{TBL})_R$ and $(I_{FBL})_R$ respectively. Similarly, after the classification of Red lesion region as $(I_{RL})_R$, the True and False Red lesion region is denoted as $(I_{TRL})_R$ and $(I_{FRL})_R$ respectively. In the second stage, the True Lesion regions are further categorized into sub-classes; for example, the True Bright Lesion regions are categorized as Hard Exudates ($(I_{TBL}^{EX})_R$) and Cotton Wool Spots ($(I_{TBL}^{CWS})_R$. Similarly, the True Red Lesion regions are categorized as Hemorrhages ($(I_{TRL}^{HM})_R$) and Microaneurysms ($(I_{TRL}^{MA})_R$). The simplified representation of classification process is shown through the following mathematical representations.

$$I_L = (I_{BL} \& I_{RL}) \tag{21}$$

where

$$I_{BL} = (I_{TBL} \& I_{FBL}) and\ I_{RL} = (I_{TRL} \& I_{FRL}) \tag{22}$$

where

$$I_{TBL} = \left(I_{TBL}^{EX} \,\&\, I_{TBL}^{CWS}\right) \; and \; I_{TRL} = \left(I_{TRL}^{MA} \,\&\, I_{TRL}^{HM}\right) \tag{23}$$

3.5 DR Grading

After classifying all the regions into different classes, their count is processed for grading the severity of DR in the given input image. The following mathematical expression shows the accumulated count of each lesion.

$$C_{\{EX,CWS\}} = \cup_R \left(I_{TBL}^{EX,CWS}\right)_R \tag{24}$$

And

$$C_{\{MA,HM\}} = \cup_R \left(I_{TRL}^{MA,HM}\right)_R \tag{25}$$

Based on the obtained count, the DR grading is formulated as function of $C_{\{EX,CWS\}}$ and $C_{\{MA,HM\}}$ as follows.

$$DG = \varphi(C_{\{EX,CWS\}} \& \; C_{\{MA,HM\}}) \tag{26}$$

where $DG \in \{0,1,2,3\}$, signifies the possible four grades of DR. DG = 3, DG = 2, DG = 1, and DG = 0 implies the severe DR, Moderate DR, Mild DR, and No DR respectively.

4 Experimental results

The performance analysis of the proposed mechanism is assessed here with numerous simulation studies with different datasets. For simulation purposes, MATLAB tool is used with image processing and statistics toolbox. Further, the system configurations include a personal computer with 8 GB RAM and a 2.4 GHz processor. Herein this section, initially, the details of datasets are explored and then the obtained results through several performance metrics.

4.1 Datasets

A standard dataset DIARETDB1 is considered for experimental validation, which are freely available and standard benchmark datasets which most researchers use for validating their methods. The details are explored here.

DIARETDB1 DIARETDB1 consists of totally 89 fundus images among which only five are in normal condition (No DR) and the remaining images have at least mild NPDR. In every image, this dataset provides ground truths for three types of lesions such as MA, HM, and Hard Exudates. To acquire the images, a digital fundus camera is placed under 50^0 field of view. This dataset is also regarded as the fundus images with calibration level.

Table 3 Confusion Matrix of 'Image016.png' with SVM

		Predicted EX	Total CWS	Predicted EX	Total CWS	Predicted EX
Actual	**EX**	**22,310**	26	0	0	22,336
	CWS	244	**17,980**	0	0	18,224
	MA	0	0	**14,340**	0	14,340
	HM	0	0	261	**19,959**	20,220
Total		22,554	18,006	14,601	19,959	**75,120**

Table 4 Confusion Matrix of 'Image016.png' with GMM

		Predicted EX	Total CWS	Predicted EX	Total CWS	Predicted EX
Actual	**EX**	**20,102**	2234	0	0	22,336
	CWS	1822	**16,402**	0	0	18,224
	MA	0	0	**12,906**	1434	14,340
	HM	0	0	2022	**18,198**	20,220
Total		21,924	18,636	14,928	19,632	**75,120**

4.2 Performance metrics

For performance assessment, a total of four performance metrics are considered namely Area Under ROC Curve (AUC), Accuracy, Specificity and Sensitivity. The mathematical expressions of these metrics are derived based on the confusion matrix which is formulated based on four metrics such as True Positive (TP), True Negative (N), False Positive (FP) and False Negative (FN).

$$Specificity = \frac{TN}{TN + FP} \times 100\% \tag{27}$$

$$Sensitivity = \frac{TP}{TP + FN} \times 100\% \tag{28}$$

$$Accuracy = \frac{TP + TN}{TP + TN + FP + FN} \times 100\% \tag{29}$$

$$AUC = \frac{1}{2}(Sensitivity + Specificity) \tag{30}$$

As this method is a hierarchical classification, the performance assessment is done under two phases; in the first phase of classification, the entire region is categorized as True lesions and False lesions. In this phase, the TP is measured as the number of True Lesions which are classified as True Lesions, FN is measured as number of True Lesions that are classified as False Lesions, FP is measured as number of False Lesions that are classified as True Lesions, and TN is measured as number of False Lesions that are classified as False Lesions. Here the true lesions are considered in both bright and red lesion

Table 5 Confusion Matrix of 'Image016.png' with k-NN

		Predicted EX	Total CWS	Predicted EX	Total CWS	Predicted EX
Actual	**EX**	**19,651**	2685	0	0	22,336
	CWS	2191	**16,033**	0	0	18,224
	MA	0	0	**12,616**	1724	14,340
	HM	0	0	2430	**17,790**	20,220
Total		21,842	18,718	15,046	19,514	**75,120**

regions. In the second phase, only true lesions are subjected to classification and hence the confusion matrix is built between sub-classes. For bright lesions, EX and CWS are considered as sub-classes and for red lesions MA and HM are considered as sub-classes.

Table 3 shows the confusion matrix of 'Image016.png' from DIARETDB1 dataset after processing it through the proposed approach with SVM. Table 4 shows the confusion matrix of 'Image016.png' after processing it through the proposed approach with GMM. Table 5 shows the confusion matrix of 'Image016.png' after processing it through the proposed approach with k-NN. From the confusion matrix, the highlighted values are termed as True positives which are almost equal to their actual count. For example, the total Lesion pixels available in a retinal image of DIARETDB1 dataset are 20,220 among which22,336 are EXs, 18,224 are CWSs, 14,340 are MAs and 20,220 are HMs. Out of 22,336 EX pixels, the proposed approach classified 22,310 as EX pixels and hence TP is 22,310. Similarly, the TPs of CWS, MAs and HMs are observed as 17,980, 14,340 and 19,959 respectively. Based on these values, the performance metrics are measured to assess the effectiveness of Lesions segmentation.

4.3 Results

Based on the results demonstrated in confusion matrix through TP, FP, FN and TNs, the performance of proposed mechanism is determined and is calculated through several performance metrics like sensitivity, specificity and AUC. To alleviate the robustness of developed mechanisms, extensive simulations with different machine learning algorithms is conducted. Three algorithms namely K-NN, GMM and SVM are used for classification purposes. For every algorithm, the feature count is varied as 5, 10, 15, 20, 25 and 30 and

Table 6 Results of Phase 1 classification: True Bright Lesions and False Bright Lesions

Number of Features	Specificity (%)			Sensitivity (%)		
	SVM	GMM	k-NN	SVM	GMM	k-NN
30	66.4492	**86.8243**	**87.2740**	**99.5940**	**90.5949**	**87.9558**
25	77.3291	85.6469	86.3253	96.4380	88.0840	85.5273
20	**77.8542**	84.6273	86.7489	96.4173	80.6440	82.4840
15	70.7440	84.6540	86.5242	92.6291	74.4053	82.4166
10	63.3274	83.4273	86.3558	90.4380	67.9140	77.0719
05	64.4173	83.2740	86.0786	68.4380	63.4173	68.0840

Table 7 Results of Phase 2 classification: EX and CWS

Number of Features	Specificity (%)			Sensitivity (%)		
	SVM	GMM	k-NN	SVM	GMM	k-NN
30	**99.8855**	**96.5422**	**98.4138**	**100**	**100**	**99.4838**
25	99.8562	96.3169	97.8516	99.5460	99.6039	97.1716
20	99.6652	95.5388	97.2187	98.4880	99.4838	96.4969
15	98.4215	95.6336	97.0845	97.3369	99.4387	89.8136
10	97.4423	94.2180	96.3276	98.2149	98.8288	89.3069
05	95.6385	94.2138	96.3049	96.3169	95.4272	83.4836

the system is trained followed by the testing phase. This kind of simulation is applied for both bright and red lesions and the results are explored clearly. Table 6 shows the results of proposed mechanism at phase 1 classification, i.e., the classification of true bright lesions and false bright lesions. Next, Table 7 shows the results of proposed mechanism at phase 2 classification, i.e., the classification of EX and CWS. From the results shown in Table 6, the maximum sensitivity (99.5940%) is observed for SVM algorithm with full feature count while the maximum specificity (87.2740%) is observed for K-NN algorithm with full feature count. Next, the minimum sensitivity (63.4173%) is observed for GMM algorithm with 5 feature count while the minimum specificity (63.3274%) is observed for SVM algorithm with 10 feature count. Further, the average specificity of proposed approach with SVM, GMM and k-NN is observed as 70.0202%, 84.7423% and 86.5511% respectively. The average sensitivity of proposed approach with SVM, GMM and k-NN is observed as 90.6591%, 77.5099% and 80.5889% respectively. From the results it is observed that in the second phase of classification, the maximum sensitivity (100%) is observed for SVM and GMM algorithms with full feature count while the maximum specificity (99.8855%) is observed for SVM with full feature count. Further, the minimum sensitivity (83.4836%) and specificity (94.2138%) are observed for the simulation of k-NN with 05 feature count and GMM with 05 feature counts respectively.

The results derived after the classification of red lesions are demonstrated in Table 8 and Table 9. From Table 8, the maximum sensitivity is observed as 78.0141% obtained at the simulation study of full feature count with k-NN algorithm. Further, the minimum sensitivity is observed as 40.2358% at SVM with 05 feature count. As the red lesions are

Table 8 Results of Phase 1 classification: True Red Lesions and False Red Lesions

Number of Features	Specificity (%)			Sensitivity (%)		
	SVM	GMM	k-NN	SVM	GMM	k-NN
30	**97.4215**	86.4524	81.0576	62.6542	75.3266	**78.0141**
25	92.1274	83.8824	84.8855	50.8824	73.1231	76.2452
20	92.4545	86.1059	86.4216	49.2855	71.0828	74.8822
15	91.2546	85.5102	86.2155	48.0125	70.1222	70.1125
10	90.3938	84.5241	84.4531	46.3352	64.9962	66.0821
05	85.5124	**80.4423**	84.8822	**40.2358**	62.2155	61.0792

Table 9 Results of Phase 2 classification: MA and HM

Number of Features	Specificity (%)			Sensitivity (%)		
	SVM	GMM	k-NN	SVM	GMM	k-NN
30	**100**	91.0016	93.2027	**98.1558**	83.3785	96.6085
25	98.7116	93.6398	92.4069	95.3069	82.2096	95.1116
20	98.4417	92.1127	92.4979	86.7078	80.9786	94.4015
15	97.6005	92.2016	91.4417	88.7076	90.1089	85.3120
10	96.3809	91.6395	91.3116	87.0888	76.4326	77.0689
05	94.8909	90.9816	91.1952	84.3073	74.8973	76.1645

similar in characteristic with vessel regions, the SVM cannot sufficiently discriminate them thereby has shown very poor detection performance. Next, the maximum specificity (97.4215%) and minimum specificity (80.4423%) are observed at SVM with full feature count and GMM with 05 feature count respectively. The average specificity of SVM, GMM and k-NN is observed as 91.5274%, 84.4862% and 84.6526% respectively. Similarly, the average sensitivity of SVM, GMM and k-NN is observed as 49.5676%, 69.4777% and 71.0692% respectively. From the values, it can be said that the k-NN algorithm had shown much better performance in the identification of red lesions from non-lesions. As the pixels at red-lesion regions have similar intensities as the pixels of non-lesion regions, the mean, variance, maximum and minimum values of these regions are slightly separated but not largely. Due to the similarity of intensities, the system recognizes red-lesions as non-lesions and results in poor sensitivity.

Next, the second phase of classification of true red lesions into HM and MA is shown in Table 9. In this phase, the maximum performance is obtained by the SVM algorithm as its average specificity and sensitivity are calculated as 97.6709% and 90.0457%. For the remaining algorithms such as GMM and k-NN, the average specificity is observed as 91.9295% and 92.0093% respectively. Similarly, the average sensitivity is observed as 81.3342% and 87.4445% for GMM and k-NN algorithms respectively. On the other hand, the maximum sensitivity (98.1558) and maximum specificity (100%) is observed at SVM with full feature count. Based on these results, it can be stated that the SVM is much better for the classification of red lesions. As the red lesions are more important attributes for the DR grading system, the accurate classification can help in the accurate diagnosis.

Figure 5 shows the AUC results obtained after the classification of bright lesions. Here, the AUC is calculated as an average of sensitivity and specificity. At the classification of true bright lesions from false bright lesions, the average AUC of k-NN, GMM and SVM is observed as 83.5705%, 81.1261% and 80.3396% respectively. Similarly, at the classification of EX from CWS, the average AUC of k-NN, GMM and SVM is observed as 94.9131%, 97.1038% and 98.4010% respectively. Next, the AUC results obtained after the classification of red lesions are shown in Fig. 6. At the classification of true red lesions from false red lesions, the average AUC of k-NN, GMM and SVM is observed as 77.8609% 76.9820% and 70.5475% respectively. Similarly, at the classification of MA from HM, the average AUC of k-NN, GMM and SVM is observed as 89.7269% 86.6319% and 93.8583% respectively.

Table 10 explores the effectiveness of the proposed automatic DR grading system by comparing it with several existing methods through different performance metrics. For comparison, the methods that used DIARETDB1 database are referred due to the

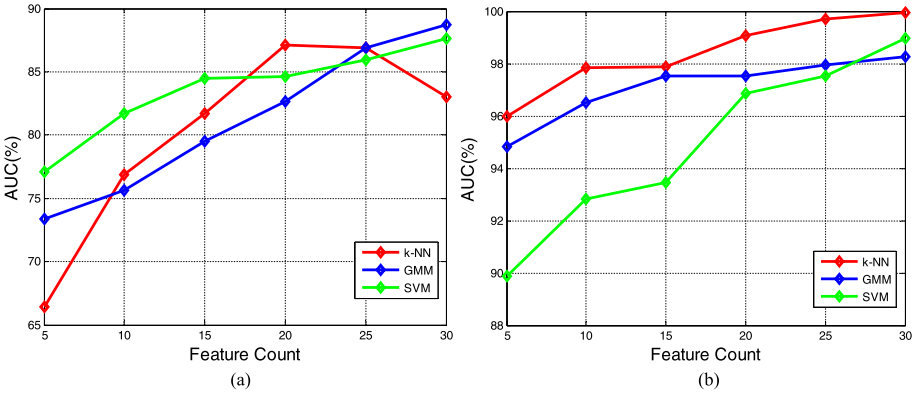

Fig. 5 (**a**) AUC at phase 1 of bright lesions and (**b**) AUC at phase 2 of bright lesions

commonality that exists between them. Among the existing methods, M. K. Fadafen [19] applied a simple mathematical morphology to segment the exudates and it gained only an AUC of 90.12%. They have mainly concentrated on classification but not on grading, which is the main limitation. Moreover, they applied pixel level classification over the entire image which is not a suggestable solution because without segmenting the vessels and OD, the lesion segmentation results in more false positives. Next, Pratt et al. [39] developed a complete DR grading system with the help of deep learning algorithms. A 13 layered CNN model was employed for feature extraction followed by classification of fundus images. However, they did not design any separate method for the removal of background regions such as vessels and OD which resulted in larger number of false positives at classification. Moreover, they did not concentrate on the quality enhancement which shows a serious impact on the DR diagnosis results. For real time images, their method showed very poor performance as it consists of several distortions and artifacts. Recently, Eman et al. [7] also developed a complete DR grading system based on multiple retinal lesions. Even though they applied different methods at different stages, they had shown limited performance because they did not differentiate between bright and red lesions. Moreover,

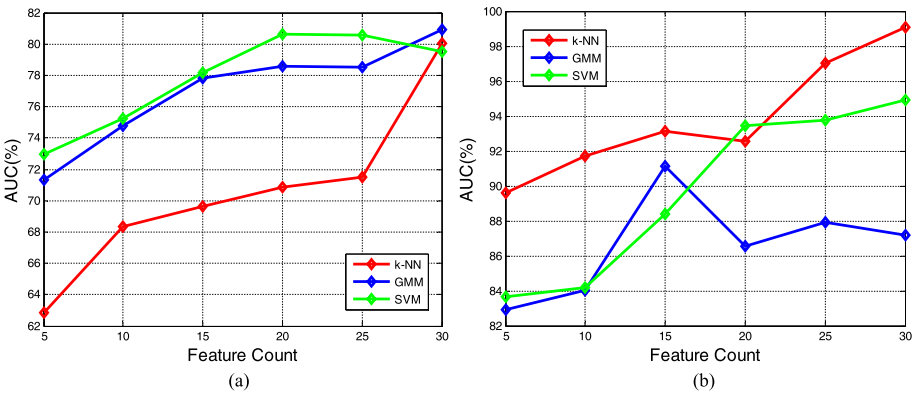

Fig. 6 (**a**) AUC at phase 1 of red lesions and (**b**) AUC at phase 2 of red lesions

Table 10 Comparison with existing methods

Author	Dataset	Focused on	Methodology	Performance
M. K. Fadafen [19]	DIARETDB1	Segmentation of EX	Mathematical Morphology	AUC—90.12%
Pratt et al. [39]	DIARETDB1	Grading of DR	13 layered CNN	Sensitivity – 91.2, Accuracy – 75%
Eman et al. [7]	DIARETDB1	Lesions Segmentation and DR grading	GLRM, SVM, and Customized U-net	Sensitivity – 86.11% Specificity – 86.80% Accuracy – 95.05%
Proposed Method	DIARETDB1	Lesions Segmentation and DR grading	Morphology, Filtering, Composite features, k-NN, GMM and SVM	Sensitivity – 95.67%, Specificity – 88.64%, Accuracy – 93.56% and AUC – 88.5%

they considered only pixel intensity-based features and extracted through GLRM. They considered only three lesions such as EX, MA and HM but not CWS which has similar characteristics with the background of retinal image. As the lesions mostly differ through their structural features, the proposed method gained a better performance compared to [7]. Moreover, the proposed approach developed a complete DR grading system which involves pre-processing, OD and vessels segmentation, and lesions classification. Hence, it gained a superior performance in all orientations compared to the existing methods.

5 Conclusion

The microvasculature present in the retinal images is unique in nature and this part of the human circulatory system can be directly visualized in a non-invasive manner and achieve the highest level of performance in determining grade of DR using automatic DR detection system. In this paper, the complete automatic DR diagnosis system is developed in four phases: namely pre-processing, background regions segmentation, lesions classification and severity grading. Unlike the existing methods which consider only a few stages, this method focused on all stages until grading of the DR present in the given input retinal image is done. For contrast enhancement a new method called SCCE is proposed which considers the mutual information between pixels of image to adjust their contrast levels. For retinal vessels segmentation, a composite features assisted Machine learning strategy is adopted and for OD segmentation, composite feature representation. Majorly, this work is aimed at grading DR with the help of lesions. After pre-processing and the removal of vessels and OD, this method extracts entire lesions which are then subjected to classification in a hierarchical fashion. Totally four types of lesions are considered such as EX, CWS, MA and HM and they are represented through a set of 30 features. Among the 30 features, 14 are structural and 16 are intensity-based features. After feature extraction, they were fed for classification to determine true and false lesions. Further, the true lesions are classified into sub-classes and applied for grading mechanism. For experimental validation, a standard DIARETDB1 dataset is considered, and the performance metrics obtained prove its outstanding performance. The proposed method outperformed the conventional methods by accurately identifying the ODP through statistical analysis to segment OD region accurately. The designed method also achieved a high level of accuracy, which is an indication of its effectiveness.

6 Work limitations

For determining the severity grading of DR, no perfect strategy is suggested. All the authors' suggestions are based on the images captured and their attributes. There is not a simple and composite grading strategy which works for all types of situations like different ages, genders etc. The proposed method was tested on limited retinal images, hence to check its robustness several retinal images with a variety of DR statuses can be used. For feature extraction, only simple transform techniques are employed. In future, advanced transformation techniques like Tunable-Q Wavelet transform, Empirical Model Decomposition, Fourier Bessel Series Expansion methods can be applied which can exploit the low frequency features effectively. This work could be expanded by incorporating deep learning

algorithms like ResNet, ImageNet, AlexNet etc. for the classification of DR and Non-DR images and determine the stages of DR.

Data availability Data sharing is not applicable to this article as no datasets were generated during the current study.

Declarations

Conflict of interest The authors declare that they have no conflict of Interest regarding this paper's publication.

References

1. American Diabetes Association (2011) Data from the 2011 national diabetes fact sheet. [Online]. Available: http://www.diabetes.org/diabetes-basics/diabetes-statistics/. Accessed April 2023
2. Congdon N, Zheng Y, He M (2012) The worldwide epidemic of diabetic retinopathy. Indian J Ophthalmol 60(5):428–431
3. Wong TY, Sabanayagam C (2020) Strategies to tackle the global burden of diabetic retinopathy: From epidemiology to artificial intelligence. Ophthalmological 243(1):9–20
4. Garg S, Davis RM (2009) Diabetic retinopathy screening update. Clinical Diabetes 27(4):140–145
5. Abramoff MD, Niemeijer M, Russell SR (2010) Automated detection of diabetic retinopathy: barriers to translation into clinical practice. Expert Rev Med Devices 7(2):287–296
6. Abràmoff MD, Niemeijer M, SuttorpSchulten MSA, Viergever MA, Russell SR, Va B, Ginneken (2008) Evaluation of a system for automatic detection of diabetic retinopathy from color fundus photographs in a large population of patients with diabetes. Diabetes Care 31(2):62–83
7. Abdelmaksoud E, El-Sappagh S, Barakat S, Abuhmed T, Elmogy M (2021) Automatic Diabetic Retinopathy Grading System Based on Detecting Multiple Retinal Lesions. IEEE Access 9:15939–15960
8. Hassan T, Akram MU, Hassan B, Nasim A, Bazaz SA (2015) Review of OCT and fundus images for detection of macular edema,. In Proc IEEE Int Conf Imag Syst Techn (IST), Sep. pp 1–4
9. Saeed MU, Oleszczuk JD (2016) Advances in retinal imaging modalities: Challenges and opportunities. World J Ophthalmol 6(2):10–19
10. Osareh A, Mirmehdi M, Thomas B, Markham R (2006) Classification and localisation of diabetic-related eye disease. In Computer Vision ECCV 2002, ser. Lecture Notes in Computer Science, vol 2353. Springer, Berlin / Heidelberg, pp 325–329
11. Li Z, Keel S, Liu C, He Y, Meng W, Scheetz J, Lee PY, Shaw J, Ting D, Wong TY, Taylor H, Chang R, He M (2018) An Automated Grading System for Detection of Vision-Threatening Referable Diabetic Retinopathy on the Basis of Color Fundus Photographs. Diabetes Care 41(12):2509–2516
12. Biran A, Bidari PS, Raahemifar K (2016) Automatic method for exudates and hemorrhages detection from fundus retinal images. Int J Comput Inf Eng 10(9):1599–1602
13 Reza AM (2004) Realization of the contrast limited adaptive histogram equalization (CLAHE) for real-time image enhancement. J VLSI Signal Process Syst Signal Image Video Technol 38(1):35–44
14. Atlas GL, Parasuraman K (2018) Detection of retinal hemorrhage from fundus images using ANFIS classifier and MRG segmentation. Biomed Res 29(7):1489–1497
15. Tang X (1998) Texture information in run-length matrices. IEEE Trans Image Process 7(11):1602–1609
16. Loris N, Sheryl B, Stefano G, Emanuele M, Tonya B (2013) Different Approaches for Extracting Information from the Co-Occurrence Matrix. PLoS ONE 8(12):e83554
17. Bay H, Andreas E, Tuytelaars T, Van Gool L (2008) SURF: Speeded up robust features. Comput Vis Image Understanding (CVIU) 110(3):346–359
18. Orlando JI, Prokofyeva E, Blaschko MB (2017) A discriminatively trained fully connected conditional random field model for blood vessel segmentation in fundus images. IEEE Trans Biomed Eng 64(1):16–27
19. Fadafen MK, Mehrshad N, Razavi SM (2018) Detection of diabetic retinopathy using computational model of human visual system. Biomed Res 29(9):1956–1960

20. Safitri DW, Juniati D (2017) Classification of diabetic retinopathy using fractal dimension analysis of eye fundus image. In: Proc of International Conf on Mathematics: Pure, Applied and Computation, Surabaya, Indonesia. AIP Publishing, pp 020011-1–11
21. Liu JZ, Zhang LD, Yue GH (2003) Fractal dimension in human cerebellum measured by magnetic resonance imaging. Biophys J 85(6):4041–4046
22. Maksoud EA, Barakat S, Elmogy M (2020) A comprehensive diagnosis system for early signs and different diabetic retinopathy grades using fundus retinal images based on pathological changes detection. Comput Biol Med 126(104039):512–542
23. Abràmoff MD, Lou Y, Erginay A, Clarida W, Amelon R, Folk JC, Niemeijer M (2016) Improved automated detection of diabetic retinopathy on a publicly available dataset through integration of deep learning. Invest Ophthalmol Vis Sci 57(13):5200–5206
24. Savoy M (2020) IDx-DR for diabetic retinopathy screening. Am Fam Physician 101(5):307–308
25. Kumar C, Puri S, Simard P (2006) High Performance Convolutional Neural Networks for Document Processing, In: Proc of Tenth International Workshop on Frontiers in Handwriting Recognition, La Baule, France, pp 1–7
26. Bellemo V, Lim ZW, Lim G, Nguyen QD, Xie Y, Yip MY, Hamzah H, Ho J, Lee XQ, Hsu W, Lee ML, Musonda L, Chandran M, Chipalo Mutati G, Muma M, Tan GSW, Sivaprasad S, Menon G, Wong TY, Ting DSW (2019) Artificial intelligence using deep learning to screen for referable and vision-threatening diabetic retinopathy in Africa: a clinical validation study. Lancet Digit Health 1(1):e35-e44
27. Kaiming H, Zhang X, Shaoqing R, Jian S (2015) Deep Residual Learning for Image Recognition, In: Proc of International Conf on Computer Vision and Pattern Recognition, Las Vegas, NA, USA, pp 770–778
28. Simonyan K, Zisserman A (2014) Very Deep Convolutional Networks for Large-Scale Image Recognition, In: Proc of International Conf on learning representations, Vancouver, BC, Canada, pp 1–14
29. Mansour RF (2018) Deep-learning-based automatic computer-aided diagnosis system for diabetic retinopathy. Biomed Eng Lett 8(1):41–57
30. Bailey DG, Johnston CT, Ma N (2008) Connected components analysis of streamed images, In: Proc of International Conf. on Field Programmable Logic and Applications, Heidelberg, pp 679–682
31. Gadekallu TR, Khare N, Bhattacharya S, Singh S, Maddikunta PKR, Ra IH, Alazab M (2020) Early detection of diabetic retinopathy using PCA-firefly based deep learning model. Electronics 9(2):1–16
32. Zou H, Xue L (2018) A selective overview of sparse principal component analysis. Proc IEEE 106(8):1311–1320
33. Hagos MT, Kant S (2019) Transfer learning-based detection of diabetic retinopathy from small dataset, arXiv:1905.07203
34. Barker M, Adam (2021) Inception V3 Deep Convolutional Architecture for Classifying Acute Myeloid / Lymphoblastic Leukemia, intel.com. Retrieved on November
35. Tymchenko B, Marchenko P, Spodarets D (2020) Deep learning approach to diabetic retinopathy detection, arXiv:2003.02261
36. Alex K, Ilya S, Geoffrey HE (2017) ImageNet classification with deep convolutional neural networks. Commun ACM 60(6):84–90
37. Mukund S, Amir N (2020) The many Shapley values for model explanation, In: Proc of International Conf on Machine Learning, PMLR, 119, pp 9269–9278
38. Xu K, Feng D, Mi H (2017) Deep convolutional neural network-based early automated detection of diabetic retinopathy using fundus image. Molecules 22(12):2054
39. Pratt H, Coenen F, Broadbent DM, Harding SP, Zheng Y (2016) Convolutional neural networks for diabetic retinopathy. Proc Comput Sci 90:200–205
40. Scotland GS, McNamee P, Fleming AD, Goatman KA, Philip S, Prescott GJ, Sharp PF, Williams GJ, Wykes W, Leese GP, Olson JA (2010) Costs and consequences of automated algorithms versus manual grading for the detection of referable diabetic retinopathy. Br J Ophthalmol 94(6):712–719
41. Devi Yeddu Aruna Suhasini, Kamsali DMC (2022) Retinal image contrast enhancement through Pixel collaboration in spatial domain. Int J Intell Eng Syst 15(3):500–513
42. Fraz M, Remagnino P, Hoppe A, Uyyanonvara B, Rudnicka A, Owen C, Barman S (2012) An ensemble classification-based approach applied to retinal blood vessel segmentation. IEEE Trans Biomed Eng 59(9):2538–2548
43. Roychowdhury S, Koozekanani DD, Parhi KK (2015) Blood Vessel Segmentation of Fundus Images by Major Vessel Extraction and Subimage Classification. IEEE J Biomed Health Inform 19(3):1118–1128
44. Li H, Chutatape O (2001) Automatic location of optic disc in retinal images. In Proc IEEE Int Conf Image Process. IEEE Xplore, pp 837–840

45. Frame A, Undrill P, Cree M, Olson J, McHardy K, Sharp P, Forrester J (1998) A comparison of computer-based classification methods applied to the detection of microaneurysms in ophthalmic fluorescein angiograms. Comput Biol Med 28(3):225–238
46 Niemeijer M, van Ginneken B, Staal J, SuttorpSchulten M, Abramoff M (2005) Automatic detection of red lesions in digital color fundus photographs. IEEE Trans Med Imaging 24(5):584–592

Publisher's Note Springer Nature remains neutral with regard to jurisdictional claims in published maps and institutional affiliations.

Springer Nature or its licensor (e.g. a society or other partner) holds exclusive rights to this article under a publishing agreement with the author(s) or other rightsholder(s); author self-archiving of the accepted manuscript version of this article is solely governed by the terms of such publishing agreement and applicable law.

Authors and Affiliations

Y. Aruna Suhasini Devi[1] · K. Manjunatha Chari[2]

✉ Y. Aruna Suhasini Devi
arunasuha@gmail.com; yarunasuhasini@cmrcet.ac.in

K. Manjunatha Chari
mkamsali@gitam.edu

[1] Dept., of Electronics and Communication Engineering, CMR College of Engineering & Technology, Hyderabad, Telangana, India

[2] Dept., of Electrical Electronics and Communication Engineering, GITAM University, Hyderabad, Telangana, India